Submitted to Acta Materialia **February 2, 2000**

Microstructural Characterization of a Directionally-Solidified Ni-33 (at. %)Al-31Cr-3Mo Eutectic Alloy as a Function of Withdrawal Rate

S. V. Raj, I. E. Locci, J. D. Whittenberger, and J. A. Salem

NASA Glenn Research Center, MS 24-1, 21000 Brookpark Road, Cleveland, OH 44135

Abstract

The Ni-33 (at. %)Al-31Cr-3Mo eutectic alloy was directionally-solidified (DS) at different rates, V_I, varying between 2.5 to 508 mm h^{-1}. Detailed qualitative and quantitative metallographic and chemical analyses were conducted on the directionally-solidified rods. The microstructures consisted of eutectic colonies with parallel lamellar NiAl/(Cr,Mo) plates for solidification rates at and below 12.7 mm h^{-1}. Cellular eutectic microstructures were observed at higher solidification rates, where the plates exhibited a radial pattern. The microstructures were demonstrated to be fairly uniform throughout a 100 mm length of the DS zone by quantitative metallography. The average cell size, $\bar{d}$, decreased with increasing growth rate to a value of 125 μm at 508 mm h^{-1} according to the relation $\bar{d}$ (μm) ≈ 465 $V_I^{-0.22}$, where V_I is in mm h^{-1}. Both the average NiAl plate thickness, $\bar{\Delta}_{NiAl}$, and the interlamellar spacing, $\bar{\lambda}$, were observed to be constant for $V_I \leq 50.8$ mm h^{-1} but decreased with increasing growth rate above this value as $\bar{\Delta}_{NiAl}$ (μm) = 61.2 $V_I^{-0.93}$ and $\bar{\lambda}$ (μm) = 47.7 $V_I^{-0.64}$, respectively. The present results are detailed on a microstructural map.

Keywords

Optical microscopy, microstructure, compounds intermetallic, directional solidification

1.0 Introduction

An attractive combination of oxidation, physical and thermal properties makes NiAl a potential candidate material to replace superalloys in turbine airfoil applications in aircraft engines. Currently, poor elevated temperature creep properties and low room temperature fracture toughness restrict their commercial use. Since there is a long history of familiarity with single crystal and directionally-solidified (DS) processing technologies among the major aircraft engine manufacturer's dating back to the 1960's, there is a potential commercial advantage in successfully developing DS NiAl eutectic alloys since it is envisioned that engine components can be fabricated from them with only small modifications to existing production methods. Thus, DS NiAl eutectic alloys, where the eutectic phases are ideally parallel to the growth direction, have been studied by several investigators in an effort to obtain an optimum combination of high elevated temperature strength and room temperature fracture toughness properties [1,2,3,4,5,6,7,8,9,10,11,12,13,14,15]. In particular, the Ni-33(at.%)Al-34Cr[1] and the Ni-33Al-(34-x)Cr-xMo alloys, where $0 \leq x \leq 6\%$, have drawn greater attention since the earlier investigations of Walter and Cline [1,2,3] demonstrated that substitution of Mo for Cr leads to a corresponding change in the fiber morphology from Cr rods to (Cr,Mo) lamellar plates when the Mo content exceeds 0.7%. This change in fiber morphology offers the possibility of improved fracture toughness and elevated temperature creep properties [9].

In their investigations on the NiAl-(Cr,Mo) eutectic alloys, Cline and Walter [2] observed that well-aligned, lamellar microstructures could be grown from the melt when the growth rates, V_I, are less than 19 mm h^{-1}. However, these growth rates are slow and it might not be economically viable for the manufacture of turbine airfoils. Although these observations were

[1] Unless otherwise mentioned, all compositions are reported in atomic percent in this paper.

not correlated with the mechanical properties of the alloys, more recent observations on the fracture toughness and elevated temperature mechanical properties of these alloys, primarily containing either 1 or 3% Mo, are encouraging and warrant further development of this alloy system [6,8,10,13,14]. However, all these earlier studies were conducted on alloys grown at a single rate. Hence, the effect of growth rate on the room temperature fracture toughness and elevated temperature strength is unknown for the NiAl/(Cr,Mo) alloys. Investigations of the effect withdrawal rates on the microstructures and mechanical properties of these alloys could have important commercial and engineering consequences, since it has been demonstrated that the solidification rate can have both beneficial and detrimental effects on the tensile strengths of DS NiAl-34Cr depending on the test temperature [1].

The present investigation was undertaken to study the effect of growth rate on the microstructures and mechanical properties of a 33Ni-33Al-31Cr-3Mo alloy in order to answer three main questions: First, how does the microstructure vary with growth rate? Second, does the elevated temperature strength show a maxima for this alloy at a critical value of the growth rate similar to observations reported on NiAl-34Cr [1]? Third, is there any significant change in the room temperature fracture toughness of the alloy with increasing growth rate? Preliminary results from this study were recently reported, where the qualitative microstructural information, elevated temperature strength and room temperature fracture toughness data were discussed [15]. These results revealed that the microstructure exhibited multiple eutectic colonies containing parallel lamellar plates at a solidification speed of 12.7 mm h^{-1}. A cellular eutectic microstructure formed at faster solidification rates, where the NiAl and (Cr,Mo) plates exhibited a radially emanating pattern from the cell interior to its boundaries

The present paper discusses the microstructural results in greater detail including presenting quantitative correlations of some of the major microstructural parameters with the withdrawal rate to compliment the earlier results [15]. These microstructural data will be correlated with observed the mechanical properties of the alloy in an attempt to elucidate the rate controlling mechanisms in a subsequent publication. Since the preliminary results presented earlier [15] revealed that the measured Al content of a rod grown at the slowest rate of 7.6 mm h^{-1} was significantly different from the nominal values, new microstructural information is now included for a fresh batch of material close to the nominal composition and grown at 7.6 mm h^{-1}.

2.0 Experimental Materials and Procedures

Ni-33Al-31Cr-3Mo eutectic pre-charge rods, 19 mm in diameter and 178 mm long, were prepared for directional solidification by induction melting a charge of appropriate weights of elemental Al, Cr, Ni and pre-alloyed Ni-50(wt.%) Mo in high purity alumina crucibles under flowing argon and cast into a copper mold. Directional solidification was achieved through a modified Bridgeman technique. The induction-melted rods were re-melted in high purity alumina tubes, where the molten metal was allowed to solidify by pulling the tube through a hole machined in a water-cooled Cu baffle. In addition to direct radiation to the Cu baffle, heat dissipation was achieved by water cooling the pull ram. The rods were grown at rates varying between 2.5 and 508 mm h^{-1} under flowing high purity argon maintained under a slightly positive pressure. Prior to melting, the chamber atmosphere was evacuated through two pump down-back fill cycles at room temperature, where a vacuum level of about 3-7 $x10^{-4}$ Pa was attained before back filling with high purity dry argon. The crucible withdrawal rate, the baffle temperature, the mid-point melt temperature and the temperature variation along the length of the crucible were monitored periodically by a computerized data acquisition and control system. The molten metal

temperature was typically 1900-1910 K, which represents a superheat of about 175 K. The measured thermal gradient, G, at the liquid/solid interface was determined to be about 8-10 K mm^{-1}. The baffle temperature was maintained at about 285 K at the beginning of each run but typically increased to ~ 297 K by the end of the run. There was no visible evidence that the molten metal had reacted with the crucible during the DS processing. Additional details of the materials processing techniques are described elsewhere [13,15].

Directionally-solidified rods 19 mm in diameter, and with a DS region approximately 100 mm long, could be produced at withdrawal rates above 7.6 mm h^{-1} within a standard 10 h run time. However, rods grown at the two slower rates of 2.5 and 7.6 mm h^{-1} produced shorter DS regions of about 20 and 50 mm, respectively, in a standard run. In this case, a detailed quantitative metallography study was not conducted on these rods since there was insufficient DS material to ensure a statistical sampling size.

Compression specimens, fracture toughness bend bars, and chemical and metallography samples were sectioned from each rod by electro-discharge machining (EDM) (Fig. 1). The locations of the specimens were carefully identified with respect to their position in the DS rod in order to correlate possible variations in the chemical composition and microstructure with the mechanical properties.

The chemical composition of both the DS and the non-DS regions were measured for each processed rod to monitor the loss of any alloying elements during directional solidification. The inductive coupled plasma (ICP) technique was used for determining the major alloying

elements and impurities. The concentrations of nitrogen and oxygen were determined by an inert gas fusion method, while carbon and sulfur were measured by the combustion extraction method.

Transverse sections were obtained from different regions of the DS zones to study the qualitative and quantitative variations in the microstructure. Optical and scanning electron microscopy (SEM) techniques in both the secondary electron (SE) and the back-scattered electron (BSE) imaging modes were used for conducting detailed metallographic observations. The constituent phases were identified by a combination of x-ray diffraction (XRD) and energy dispersive spectroscopy (EDS) and x-ray dot mapping techniques.

Quantitative metallographic measurements were made on micrographs of transverse sections by measuring the cell sizes and the NiAl plate thickness along randomly-oriented test lines. Individual measurements were made on representative micrographs photographed from the top, middle and bottom of each DS rod, where "bottom" denotes the region closest to the DS/non-DS interface and "top" represents the location of the ingot close to the last solidification zone (Fig. 1). Since both planar eutectic and cellular microstructures were observed in this study, the linear intercept technique was chosen for its simplicity in the determination of the microstructural parameters. As discussed in § 3.2, the NiAl and (Cr,Mo) spacing in the cell interior was finer than those between neighboring cells. This region with a finer interlamellar spacing is defined as the cell size in this paper, while the region between neighboring cells with a coarser interlamellar spacing is defined as the intercellular width. Owing to the radial nature of lamellae within the cells, the length of the test line was chosen to ensure that it commenced and terminated at a NiAl/(Cr,Mo) boundary. Care was also taken to ensure that the orientation of the test line was not parallel to those of the lamellae.

The mean cell size, $\bar{d}$, was measured by averaging the individual intercept lengths, Δ_i along several randomly-oriented test lines, where each test line commenced and terminated at an intercellular region. The mean width of the intercellular region, $\bar{\delta}$, was then determined from these measurements. The edge-to-edge intercept thickness of each NiAl plate, Δ_{NiAl}, was measured along a randomly-oriented test line. The mean thickness of the NiAl phase, $\bar{\Delta}_{NiAl}$, reported in this paper represents an average value of the measured intercept spacing along several test lines. The mean intercept spacing, $\bar{\lambda}$, at each growth rate was then determined from these intercept measurements. The error reported in this paper represent 95% confidence limits.

3.0 Results and Discussion

3.1 Chemical composition of the directionally-solidified and induction–melted materials

Table 1 compares the composition of the DS and the non-DS regions of each rod for different withdrawal rates. It should be noted that the relative errors in these determinations are about 5% for the major elements and about 10% for the interstitial elements. The sulfur content was less than < 0.0001 wt. % in all cases. The compositions of all the alloys were close to the nominal values for the major elements indicating that there was practically little or no loss of Al and Cr during processing. An examination of Table 1 reveals that significant amounts of Si was picked up during the DS processing run presumably from the alumina tube. Significant amounts of Cu, varying between 80 and 430 at. p.p.m., were also picked-up during the preparation of the pre-charge by induction melting presumably due to a reaction of the molten metal with the Cu mold. In addition, small amounts of Fe were observed in the induction-melted material, where this element varied between 5 and 65 at. p.p.m. The source of this contaminant was attributed to

the elemental Cr used in the preparation of the alloys, which had a Fe content of about 40 p.p.m. The source of the carbon contamination was probably due to the graphite susceptors utilized in both the induction melting and DS processing equipment. It was more difficult to account for the source of the oxygen pick-up during directional solidification, which may be due to the presence of remnant moisture in the chamber after pump down.

3.2 Evaluation of the spatial variation in the microstructure

Since the thermal gradient may have varied during directional solidification especially at the slower withdrawal rates, it was necessary to examine the DS rods for variations in the microstructure. Transverse slices cut from the top, middle and bottom sections of each rod did not reveal any significant variations in the microstructure along the length of the DS zone (Fig. 2). Although the microstructure was constant along the length of the DS region, it varied with the solidification rate. A planar eutectic microstructure was observed at growth rates less than 12.7 mm h^{-1}, where the boundaries of the eutectic colonies were easily discernible due to a change in the orientation of the lamellae at colony boundaries (Figs. 2(a), 3(a) &(b)). However, the (Cr,Mo) (light phase) and the NiAl (dark phase) plates were approximately parallel to each other within each colony. Growth faults were also commonly observed (e.g. arrow in Fig. 3(a)).

Cellular microstructures were observed with the (Cr,Mo) and NiAl plates emanating radially from the cell interior to the cell boundaries above a growth rate of 12.7 mm h^{-1} (Figs. 2(b)-(d)). At a growth rate of 25.4 mm h^{-1}, the intercellular regions were faintly discernable in many areas of the specimen, although they were distinct in some regions (Fig. 2(b). In this case, there was only a gradual variation in the interlamellar spacing from the cell interior to the boundaries. At faster withdrawal rates, the intercellular regions were clearly defined primarily

because of a dramatic increase in the interlamellar spacing near their boundaries (e.g. arrows in Figs. 2(c)).

On close examination, this increase in spacing was observed to occur due to a fusion of neighboring (Cr,Mo) plates within the cells as they approached the boundaries (e.g. circled areas in Fig. 2(c) & (d)). These joining of the (Cr, Mo) plates resulted in the formation of a "tuning fork" morphology in the intercellular regions. Significantly, the (Cr,Mo) plates that did reach the intercellular boundaries were intact although they were much thicker than those within the cells. This morphology suggests that these boundaries may still be able to provide some resistance to an advancing crack although the lines of separation between the cells are the likely weak points in this alloy.

The longitudinal microstructures of the rods grown between 7.6 and 508 mm h^{-1} showed that both the planar eutectic colonies and the cellular grains were several millimeters in length along the growth direction. Examples of these microstructures are shown in Figs. 4(a-d) for growth speeds of 12.7, 25.4, 127 and 254 mm h^{-1}, respectively. The orientation of the lamellae was not always parallel to the growth direction (e.g. Fig. 4(a)). Observations of the intercellular regions at higher magnifications revealed that the (Cr,Mo) plates were often inclined or perpendicular to the growth axis of the adjacent cells thereby suggesting that they would provide barriers to crack propagation in the boundaries. Microstructural instabilities, similar to those predicted by theory [16], were observed at 25.4 (Fig. 4(b)) and 50.8 mm h^{-1} throughout the length of the DS zone. These oscillating instabilities are expected to provide a tortuous path for crack propagation along the cell boundaries.

3.3 Effect of withdrawal rate on the cell size and the width of the intercellular region

Figure 5 shows the typical distribution in the cell sizes for $V_t = 25.4$, 127 and 508 mm h^{-1}, where the population size varied between 99 and 280 cells. It is evident that the cell size follows a near-Gaussian distribution for each solidification rate although it exhibits a slight tendency to skew to the right at the lower growth rates. The distribution is somewhat tighter at the faster withdrawal rates.

The average cell sizes measured at the top, middle and bottom of each DS rod decreased with increasing growth rate before becoming constant when $V_t \geq 254$ mm h^{-1} (Fig. 6(a)). Figure 6(a) indicates that the cell size decreases rapidly from about 240 μm at 25.4 mm h^{-1} towards a value of about 125 μm at 254 mm h^{-1}. Walter and Cline [1] also qualitatively observed that the cell size decreased with increasing solidification rate in a NiAl-34Cr alloy exhibiting a rod-like eutectic microstructure although they did not report any quantitative microstructural data. Although there was some apparent variation in the cell size along the length of each rod, which was somewhat larger at 25.4 mm h^{-1} than at 508 mm h^{-1}, it was still within the observed experimental scatter. This observation is significant since it suggests that good microstructural control should be possible during a typical DS production run of this alloy in the manufacture of an airfoil. In contrast to the cell size, the width of the intercellular region was essentially independent of the growth rate, where the width of the intercellular region varied between 20 and 25 μm (Fig. 6(b)).

Figure 6 (c) shows a double logarithmic plot of the mean values of the cell size and width of the intercellular regions against the withdrawal rate. A regression line through the cell size data resulted in the following relationship:

$$\bar{d} = \left(\frac{464.5}{V_I^{0.22}}\right) \quad (\mu m) \quad (R_d^2 = 0.81) \quad (\text{for } V_I \geq 25.3 \text{ mm h}^{-1}) \qquad (1)$$

where R_d^2 is the coefficient of determination and V_I is in mm h^{-1}. As expected from the trend depicted by the local microstructure (Fig. 6(b)), the average width of the intercellular region also did not exhibit any strong dependency on withdrawal rate (Fig. 6(c)). This observation, coupled with the decrease in the cell size with increasing solidification rate, effectively increases the area fraction of the cell boundaries, A_b, from about 10% at 12.7 mm h^{-1} to a constant value of about 15% at 508 mm h^{-1} (Fig. 6(d)).

The formation of cells and dendrites occur due to perturbations at the liquid-solid interface during solidification thereby resulting in a non-planar interface. It has been demonstrated in non-eutectic superalloys that the primary dendrite arm or cell spacing is proportional to $V_I^{-0.25} G^{-0.5}$ [17], where G is the temperature gradient in the liquid, which is in reasonable agreement with theory [18]. Although these theoretical analyses do not necessarily apply to complex multi-component eutectic systems, where the diffusion of several elements into two or more phases comprising the eutectic microstructure make the analysis fairly complex [18,19,20], it is interesting to note that eqn. (1) does suggest that approximately $\bar{d} \propto V_I^{-0.25}$.

3.4 Variation of the NiAl plate thickness and the interlamellar spacing with growth rate

Figure 7 shows the distribution in the NiAl plate thickness (i.e. Δ_{NiAl}) in each DS rod observed at withdrawal speeds varying between 12.7 and 508 mm h^{-1}, where the sampling size varied between 410 and 1710. As illustrated in Fig. 7, the NiAl plate thickness and the spread in the distribution decreased with increasing solidification rate. The thickness of the NiAl plates

measured at the top, middle and bottom sections of each DS rod were fairly similar and did not change significantly with location.

The effect of the withdrawal speed on the average NiAl plate thickness and the mean interlamellar spacing is shown double logarithmically in Fig. 8. An examination of the data reveals that $\bar{\Delta}_{NiAl}$ and $\bar{\lambda}$ appear to be constant at about 1.5 and 3.8 μm, respectively, below a growth speed of 50.8 mm h^{-1} but decrease with increasing withdrawal speed to about 0.2 and 0.8μm, respectively, at 508 mm h^{-1}. A power-law regression to the data for V_I > 25.4 mm h^{-1} resulted in the following equations:

$$\bar{\Delta}_{NiAl} = 61.2\ V_I^{-0.93} \quad (\mu m) \quad (R_d^2 = 0.95) \qquad (2)(a)$$

$$\bar{\lambda} = 47.7\ V_I^{-0.64} \quad (\mu m) \quad (R_d^2 = 0.89) \qquad (2)(b)$$

Walter and Cline [1] observed that $\bar{\lambda}^2 V_I$ was constant for growth speeds varying between 6.3 and 762 mm h^{-1} for a NiAl-34Cr eutectic alloy. Equation (2)(b) is in reasonable agreement with these earlier results. Although the relationship $\bar{\lambda}^2 V_I$ = constant was predicted by Jackson and Hunt [19] for planar binary eutectic alloys and confirmed by experimental observations [17], it is curious that the same relationship appears to hold even for a cellular microstructure.

Since the average cell size, the average NiAl plate thickness and the mean interlamellar spacing are dependent on the withdrawal rate through eqns. (1), 2(a) and (2)(b), respectively, both $\bar{\Delta}_{NiAl}$ and $\bar{\lambda}$ can be correlated with $\bar{d}$. This correlation is shown in Fig. 9, where $\bar{\Delta}_{NiAl}$ and $\bar{\lambda}$ are observed to exhibit a linear dependence on the average cell size given by

$$\bar{\Delta}_{NiAl} = 1.4 \times 10^{-2}\ \bar{d} - 1.5 \quad (\mu m) \quad (R_d^2 = 0.92) \qquad (3)(a)$$

$$\bar{\lambda} = 2.5 \times 10^{-2}\ \bar{d} - 1.9 \quad (\mu m) \quad (R_d^2 = 0.86) \qquad (3)(b)$$

Although Fig. 9 suggests that the correlation between $\bar{\lambda}$ and $\bar{d}$ is somewhat steeper than that between $\bar{\Delta}_{NiAl}$ and $\bar{d}$, it is doubtful if this observation represents a genuine trend since $\bar{\lambda}$ was derived from $\bar{\Delta}_{NiAl}$. The linear nature of the relationship observed in Fig. 9 suggests that the diffusion kinetics determining the cell and plate formation are identical.

3.5 Re-evaluation of the microstructure map for NiAl/(Cr,Mo) eutectic alloys

Figure 10 compares the present microstructural observations, as well as those observed by us on a Ni-33Al-33Cr-1Mo alloy [21], with those reported by Cline and Walter [2] on a plot of V_I against the molybdenum content in the alloy. It is evident from this comparison that our observations are only in partial agreement with those made by Cline and Walter [2]. All three studies report nearly identical results when $V_I \leq 12.7$ mm h^{-1} for alloys containing 1 and 3% Mo. However, Cline and Walter [2] observed dendrites at higher growth speeds when $V_I \geq 12.7$ mm h^{-1}, which considerably differs from our observations of a cellular eutectic microstructure (e.g. Fig. 2). The reason for this discrepancy could stem from differences in the thermal gradients as well as in the impurity content of the alloys processed in the two studies. Cline and Walter [2] reported that their thermal gradient was 10 K mm^{-1}, and it must be concluded that their microstructures may have been influenced by impurities.

It should be noted that the elevated temperature strength and room temperature fracture toughness of alloys grown with cellular microstructures are comparable, if not slightly better, than those with a planar eutectic microstructure [15]. Figure 10 clearly indicates that cells and plates can form over a wide range of growth rates and there is a significant processing window for obtaining these microstructures. However, Fig. 10 demonstrates that only the cellular microstructures can be grown at commercially viable growth rates. The development of cellular microstructures is also relevant since alloying the alloy to improve its mechanical properties will most likely lead to a non-planar eutectic microstructure.

4.0 Summary and Conclusions

Directionally-solidified Ni-33Al-31Cr-3Mo rods were grown at rates, V_I, between 2.54 and 508 mm h^{-1}. A detailed microstructural analysis revealed that there was a transition from planar to cellular eutectic microstructures when the solidification rate exceeded 12.7 mm h^{-1}. The microstructures were demonstrated to be fairly uniform throughout a 100 mm length of the DS zone by quantitative metallography. Quantitative metallographic analysis showed that the average cell size, $\bar{d}$, decreased with increasing values of V_I, with $\bar{d} \approx 465\ V_I^{-0.22}$. Both the average NiAl plate thickness, $\bar{\Delta}_{NiAl}$, and the average interlamellar spacing, $\bar{\lambda}$, were observed to be constant for $V_I \leq 50.8$ mm h^{-1} but decreased with increasing growth rate above this value as $\bar{\Delta}_{NiAl} = 61.2\ V_I^{-0.93}$ and $\bar{\lambda} = 47.7\ V_I^{-0.64}$, respectively. The present microstructural observations are detailed in a microstructure map and compared with those reported by Cline and Walter [2]. It is demonstrated that while our observations are in excellent agreement with those reported earlier [2] for $V_I \leq 12.7$ mm h^{-1}, no dendrites were observed at higher solidification rates. It is concluded that there is a significant processing window for obtaining cellular and planar eutectic microstructures.

Acknowledgements

Th authors acknowledge the contributions of Mr. Bill Armstrong, Mr. Pete Eichele, Ms. Mr. Dereck Johnson, Mr. Myles McQuater, Ms. Theresa Nawalaniec, and Mr. Joe Sweeney for their assistance.

References

1. J. L. Walter and H. E. Cline, *Metall. Trans.* **1**, 1221 (1970).

2. H. E. Cline and J. L. Walter, *Metall. Trans.* **1**, 2907 (1970).

3. H. E. Cline, J. L. Walter, E. Lifshin and R. R. Russell, *Metall. Trans.* **2**, 189 (1971).

4. J. Klöwer and G. Sauthoff, *Z. Metallkde*, **82**, 510 (1991).

5. R. Darolia, D. F. Lahrman, R. D. Field, J. R. Dobbs, K. M. Chang, E. H. Goldman and D. G. Konitzer, *Ordered Intermetallics - Physical and Mechanical Behavior*, C. T. Liu, R. W. Cahn and G. Sauthoff, eds. (Kluwer Academic Publishers, Dordrecht, The Netherlands), pp. 679-698 (1992).

6. D. R. Johnson, X. F. Chen, B. F. Oliver, R. D. Noebe and J. D. Whittenberger, *Intermetallics* **3**, 99 (1995).

7. W. S. Walston and R. Darolia, *Structural Intermetallics-1997*, M. V. Nathal, R. Darolia, C. T. Liu, P. L. Martin, D. B. Miracle, R. Wagner and M. Yamaguchi, eds. (The Minerals, Metals & Materials Society, Warrendale PA), pp. 613-619 (1997).

8. T. M. Pollock and D. Kolluru, *Micromechanics of Advanced Materials: A Symposium in Honor of Professor James' Li's 70th Birthday*, S. N. G. Chu, P. K. Liaw, R. J. Arsenault, K. Sadananda, K. S. Chan, W. W. Gerberich, C. C. Chau and T. M. Kung, eds. (The Minerals, Metals & Materials Society, Warrendale PA), pp. 205-212 (1995).

9. J. M. Yang, *JOM* **49**, 40 (1997).

10. J. M. Yang, S. M. Jeng, K. Bain and R. A. Amato, *Acta Mater.* **45**, 295 (1997).

11. A. Misra, Z. L. Wu, M. T. Kush and R. Gibala, *Mater. Sci. Eng.* **A239-240**, 75 (1997).

12. D. V. Kolluru and T. M. Pollock, *Acta Mater.* **46**, 2859 (1998).

13. S. V. Raj, I. E. Locci and J. D. Whittenberger, *Creep Behavior of Advanced Materials for the 21st Century,* R. S. Mishra, A. K. Mukherjee and K. Linga Murty, eds., (The Minerals, Metals & Materials Society, Warrendale PA), pp. 295-310 (1999).

14. I. E. Locci, S. V. Raj, J. D. Whittenberger, J. A. Salem and D. J. Keller, *High-Temperature Ordered Intermetallic Alloys VIII,* E. P. George, M. Yamaguchi and M. J. Mills, eds., **vol. 552,** (Materials Research Society, Pittsburgh, PA), pp. KK8.1.1 (1999).

15. J. D. Whittenberger, S. V. Raj, I. E. Locci and J. A. Salem, *Intermetallics* **7**, 1159 (1999).

16. A. Karma and A. Sarkissan, Metall. Mater. Trans. **27A**, 635 (1996).

17. M. McLean, Directionally Solidified Materials for High Temperature Service, The Metals Society, London, U.K. (1983).

18. R. Trivedi, Metall. Trans. **15A**, 977 (1984).

19. K. A. Jackson and J. D. Hunt, Trans AIME **236**, 1129 (1966).

20. M. D. Rinaldi, R. M. Sharp and M. C. Flemings, Metall. Trans. **3**, 3133 (1972).

21. S. V. Raj, I. E. Locci, J. D. Whittenberger and J. A. Salem, unpublished research, NASA Glenn Research Center, Cleveland, OH (1999).

Table 1. Chemical compositions of the DS and non-DS regions of the Ni-33Al-31Cr-3Mo Alloys

Growth Rate (mm h^{-1})	Processing condition	Chemical composition (at. %)							
		Ni	Al	Cr	Mo	Si	C	N	O
7.6	DS	32.4	33.3	31.2	2.9	0.053	0.0819	0.0012	0.0071
	Non-DS	32.4	33.5	31.0	3.0	0.097	0.0662	0.0013	0.0147
12.7	DS	31.6	33.0	32.2	2.8	0.160	0.0700	0.0041	0.0300
	Non-DS	32.4	33.3	31.1	3.0	0.013	0.0737	0.0071	0.0695
25.4	DS	32.1	34.0	30.7	2.9	0.170	0.0560	0.0003	0.0150
	Non-DS	32.5	33.1	31.4	2.9	0.026	0.0644	0.0037	0.0558
50.8	DS	32.1	33.9	30.8	2.9	0.180	0.0560	0.0003	0.0200
	Non-DS	32.2	34.2	30.6	2.9	0.003	0.0410	0.0018	0.0224
127	DS	32.5	32.7	31.6	3.1	0.080	0.0430	0.0049	0.0560
	Non-DS	31.8	33.9	31.3	3.0	0.045	0.0387	0.0020	0.0476
254	DS	32.8	32.8	31.2	3.0	0.120	0.0640	0.0042	0.0230
	Non-DS	31.9	34.0	30.9	3.0	0.022	0.0570	0.0018	0.0385
508	DS	32.2	34.0	30.5	3.0	0.210	0.0560	0.0015	0.0440
	Non-DS	32.4	33.9	30.6	2.9	0.034	0.0448	0.0011	0.0361

Note:

1) Chemical analysis was not conducted on the rod grown at 2.5 mm h^{-1} since it was not used in the mechanical property characterization studies.
2) S < 0.0001 wt.% in all the alloys.
3) Cu varied between 80 and 430 at. p.p.m. in the alloys.
4) Fe varied between 5 and 65 at. p.p.m. in the alloys.

Figure Captions

Fig. 1 Schematic machining diagram showing the locations of the chemical, compression, fracture toughness and metallography specimens in relation to the directionally-solidified rod.

Fig. 2 Optical micrographs of transverse slices taken from the top (T), middle (M) and bottom (B) sections of directionally-solidified Ni-33Al-31Cr-3Mo rods grown at (a) 12.7, (b) 25.4, (c) 127 and (d) 254 mm h^{-1}. The arrows in (c) demarcate the intercellular regions. The broken circles show examples of the fusion of the (Cr,Mo) plates near the cell boundaries.

Fig. 3 Optical micrographs of transverse sections showing the planar eutectic microstructures in rods solidified at (a) 2.5 and (b) 7.6 mm h^{-1}. The arrow identifies an example of a growth fault in (a).

Fig. 4 Optical micrographs of longitudinal sections showing the microstructures of alloys grown at (a) 12.7, (b) 25.4, (c) 127 and (d) 254 mm h^{-1}. The arrow indicates the growth direction.

Fig. 5 Typical histograms showing the distribution of the average cell sizes measured in alloys grown at 25.4, 127 and 508 mm h^{-1}.

Fig. 6 The variation of (a) the average cell size and (b) the average width of the intercellular region as a function of growth rate in the top, middle and bottom sections of directionally-solidified Ni-33Al-31Cr-3Mo rods. (c) Double logarithmic plot of the average cell size and the average width of the intercellular region with growth rate, and (d) the variation of the area fraction

of the cell boundaries with growth rate in directionally-solidified solidified Ni-33Al-31Cr-3Mo rods.

Fig. 7 Comparison of the distribution in the intercept NiAl plate thickness in directionally-solidified Ni-33Al-31Cr-3Mo at different growth rates: (a) 12.7, (b) 25.4, (c) 50.8, (d) 127 (e) 254 and (f) 508 mm h^{-1}.

Fig. 8 Double logarithmic plot of the average NiAl plate thickness and the mean interlamellar spacing in directionally-solidified Ni-33Al-31Cr-3Mo rods as a function of growth rate.

Fig. 9 Correlation between of the average NiAl plate thickness and the mean interlamellar spacing with the average cell size in directionally-solidified Ni-33Al-31Cr-3Mo rods.

Fig. 10 Plot of the solidification rate against the molybdenum content in Ni-33Al-(34-x)Cr-xMo alloys, where x is the amount of Mo, demarcating the conditions under which cellular, planar and rod-like eutectic microstructures were observed. The data reported by Cline and Walter [2], as well as recent observations on Ni-33Al-33Cr-1Mo [21], are also shown.

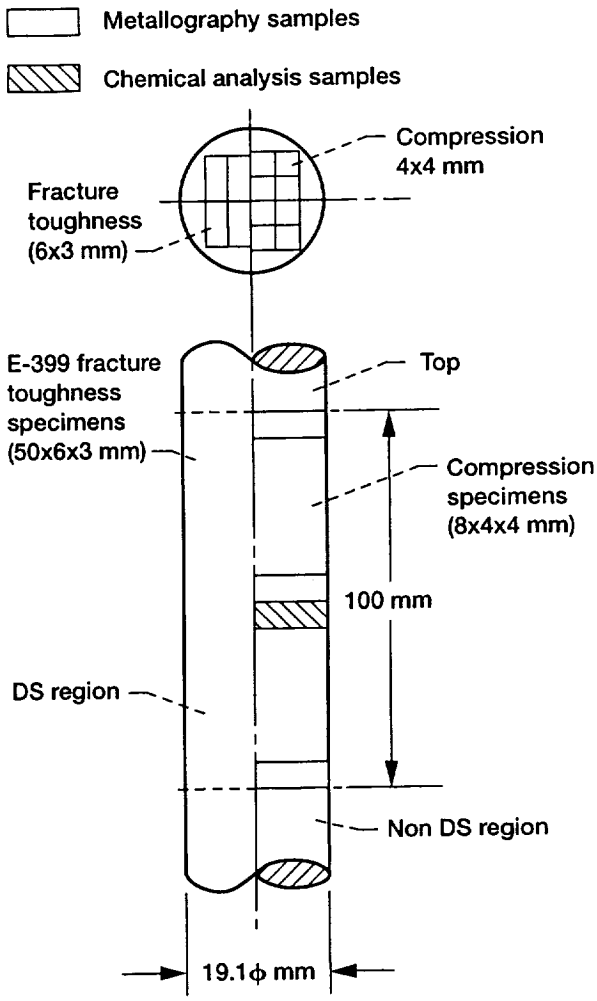
Metallography samples
Chemical analysis samples
Compression
4x4 mm
Fracture
toughness
(6x3 mm)
E-399 fracture
toughness
specimens
(50x6x3 mm)
Top
Compression
specimens
(8x4x4 mm)
100 mm
DS region
Non DS region
19.1ϕ mm

Fig. 1.

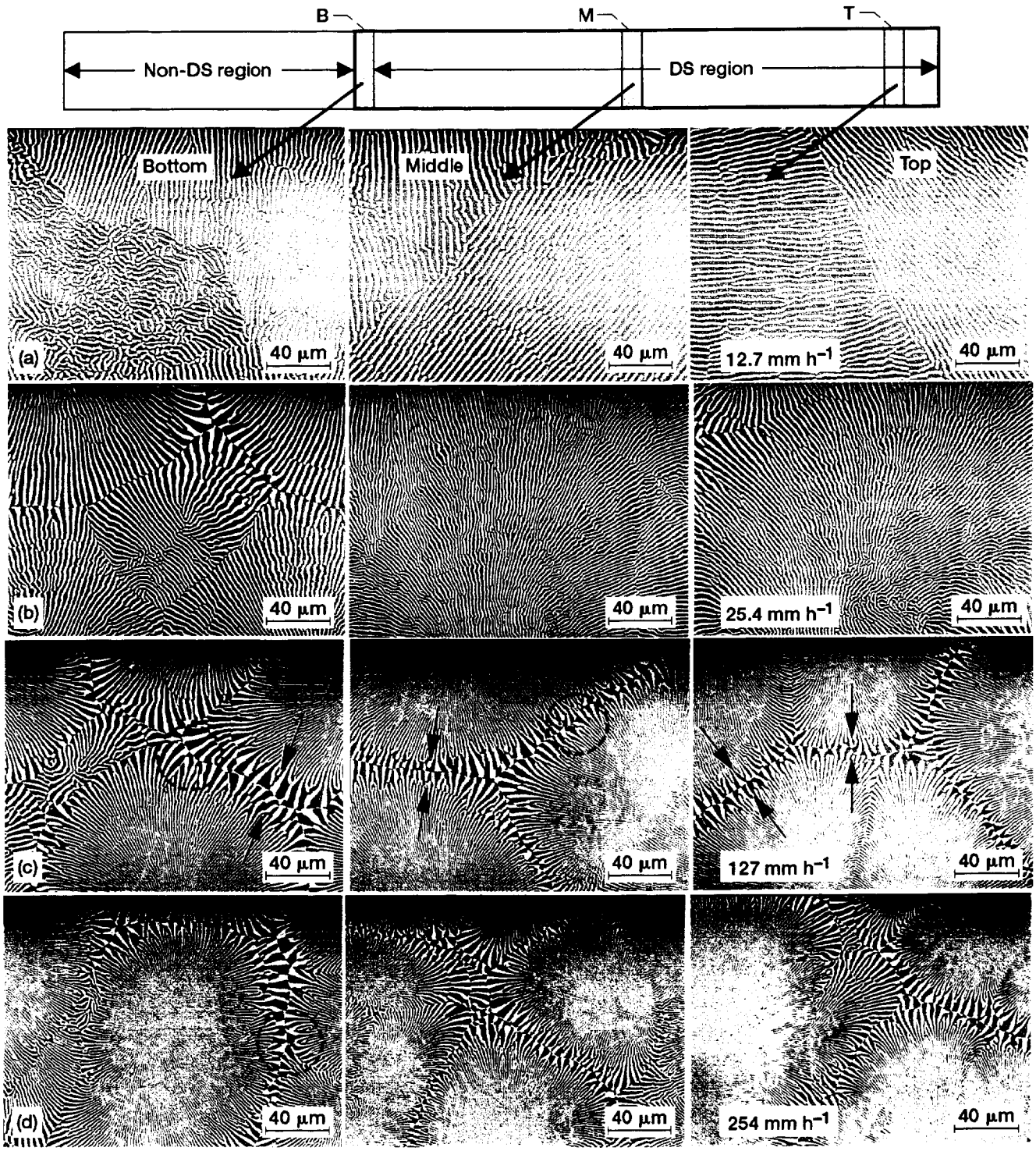
B
M
T
Non-DS region
DS region
Bottom
Middle
Top
(a)
40 μm
40 μm
12.7 mm h⁻¹
40 μm
(b)
40 μm
40 μm
25.4 mm h⁻¹
40 μm
(c)
40 μm
40 μm
127 mm h⁻¹
40 μm
(d)
40 μm
40 μm
254 mm h⁻¹
40 μm

FIG. 1

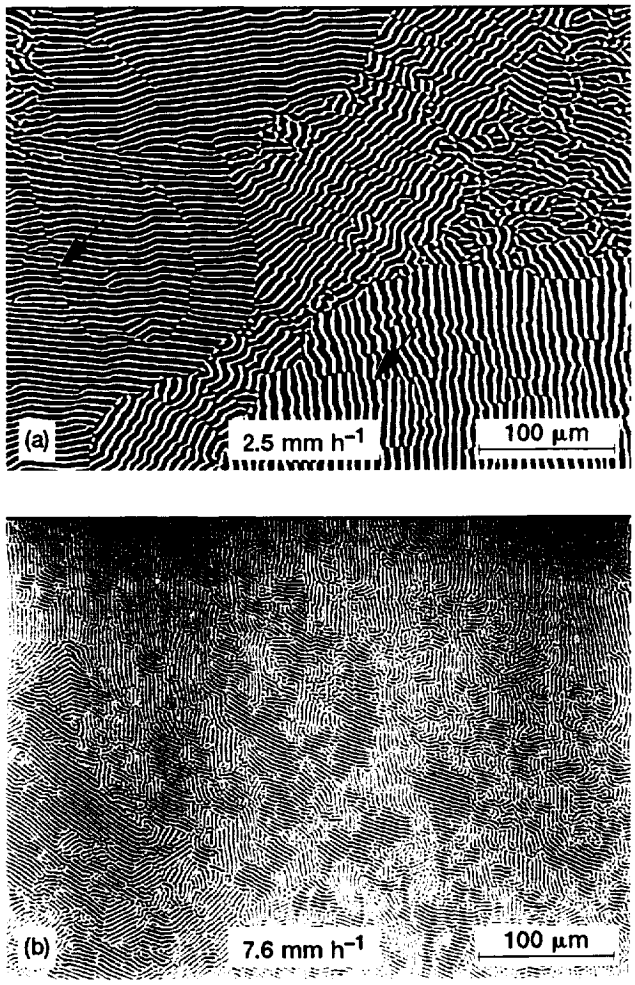

FIG. 3

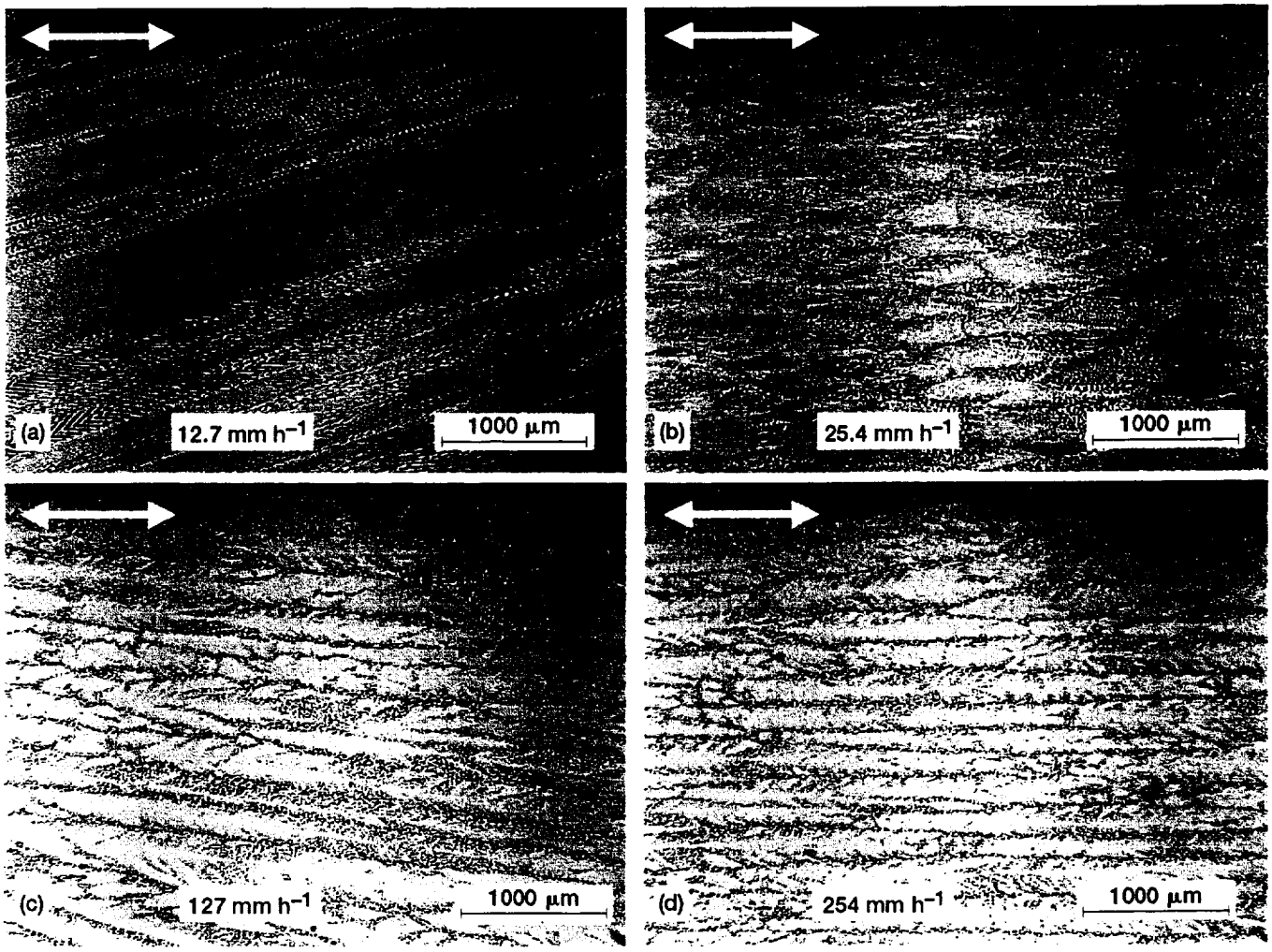
(a)
12.7 mm h^{-1}
1000 μm
(b)
25.4 mm h^{-1}
1000 μm
(c)
127 mm h^{-1}
1000 μm
(d)
254 mm h^{-1}
1000 μm

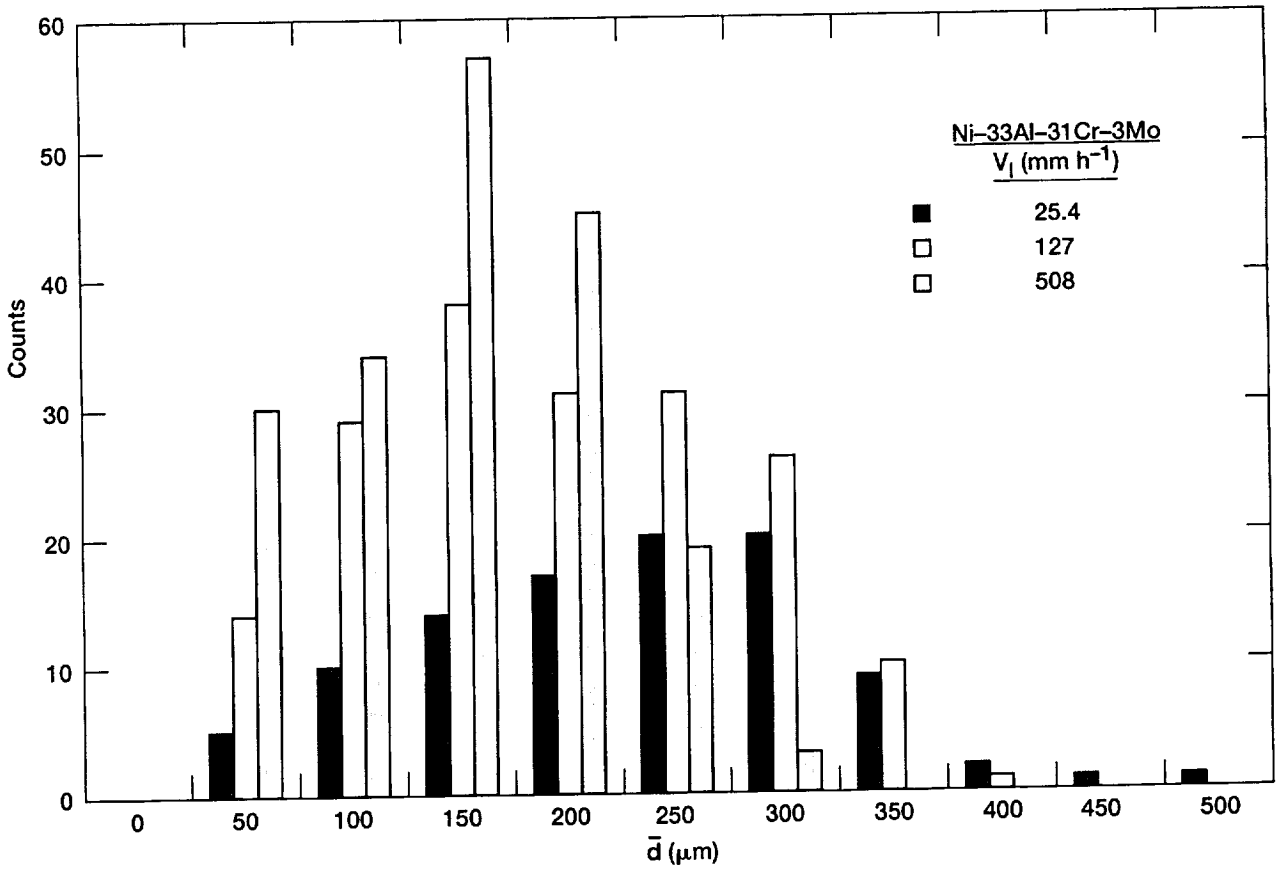
Ni–33Al–31Cr–3Mo
V_I (mm h^{-1})
25.4
127
508
Counts
0
10
20
30
40
50
60
0
50
100
150
200
250
300
350
400
450
500
$\bar{d}$ (μm)

Fig. 5.

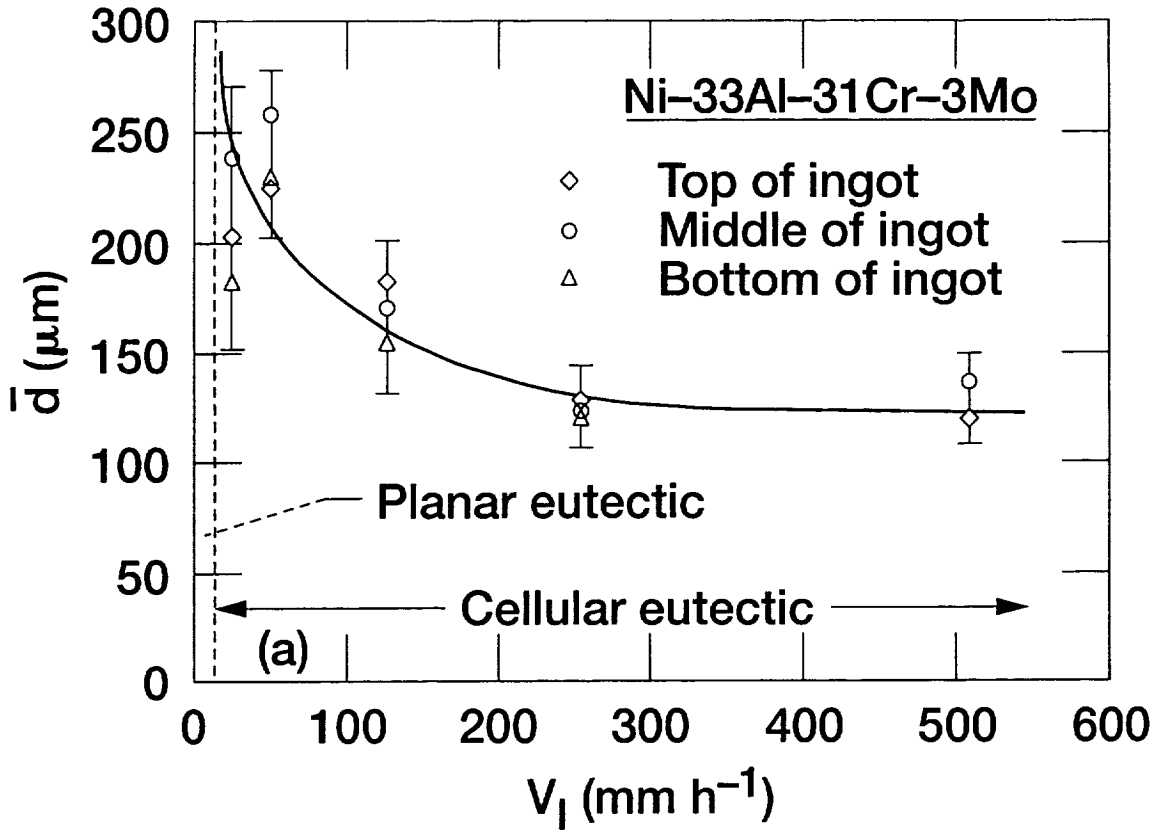
Ni–33Al–31Cr–3Mo
Top of ingot
Middle of ingot
Bottom of ingot
Planar eutectic
Cellular eutectic
(a)
$\bar{d}$ (μm)
V_I (mm h^{-1})
0
50
100
150
200
250
300
0
100
200
300
400
500
600

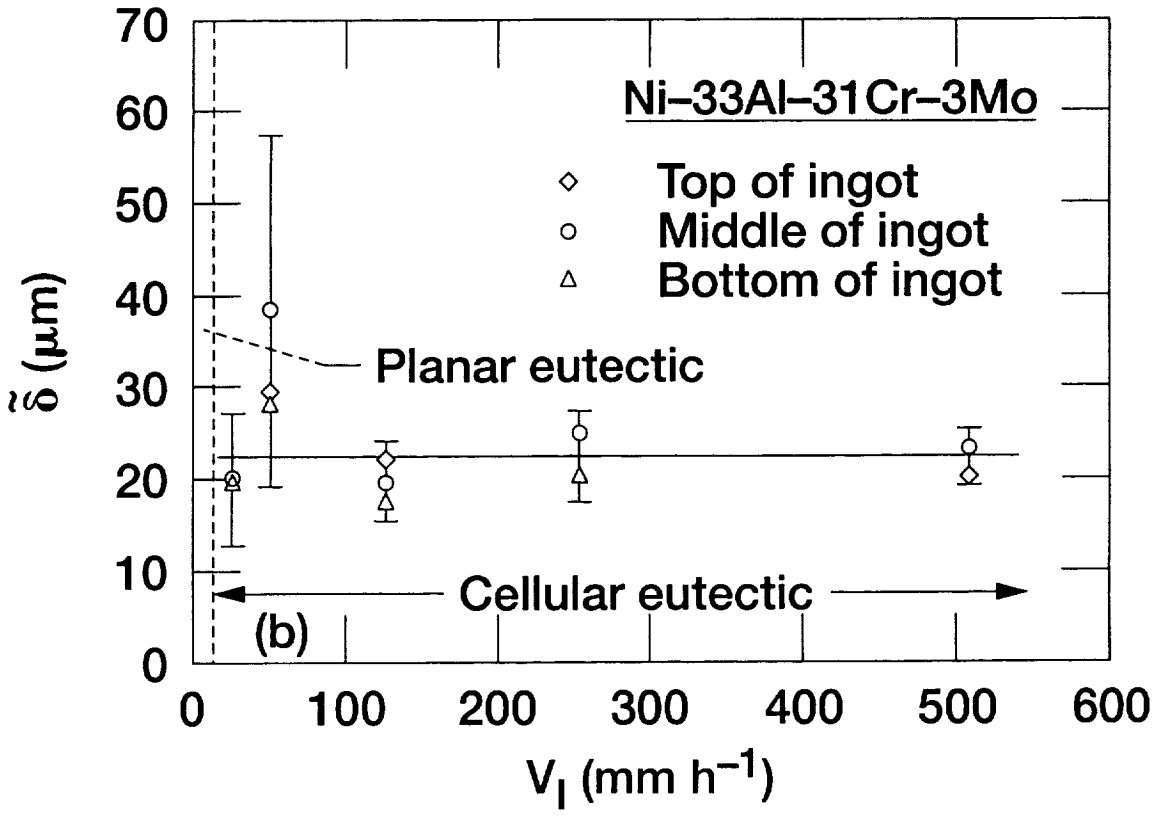
Ni–33Al–31Cr–3Mo
Top of ingot
Middle of ingot
Bottom of ingot
Planar eutectic
Cellular eutectic
(b)
$\bar{\delta}$ (μm)
V_I (mm h^{-1})
0
10
20
30
40
50
60
70
0
100
200
300
400
500
600

Fig. 6a, b.

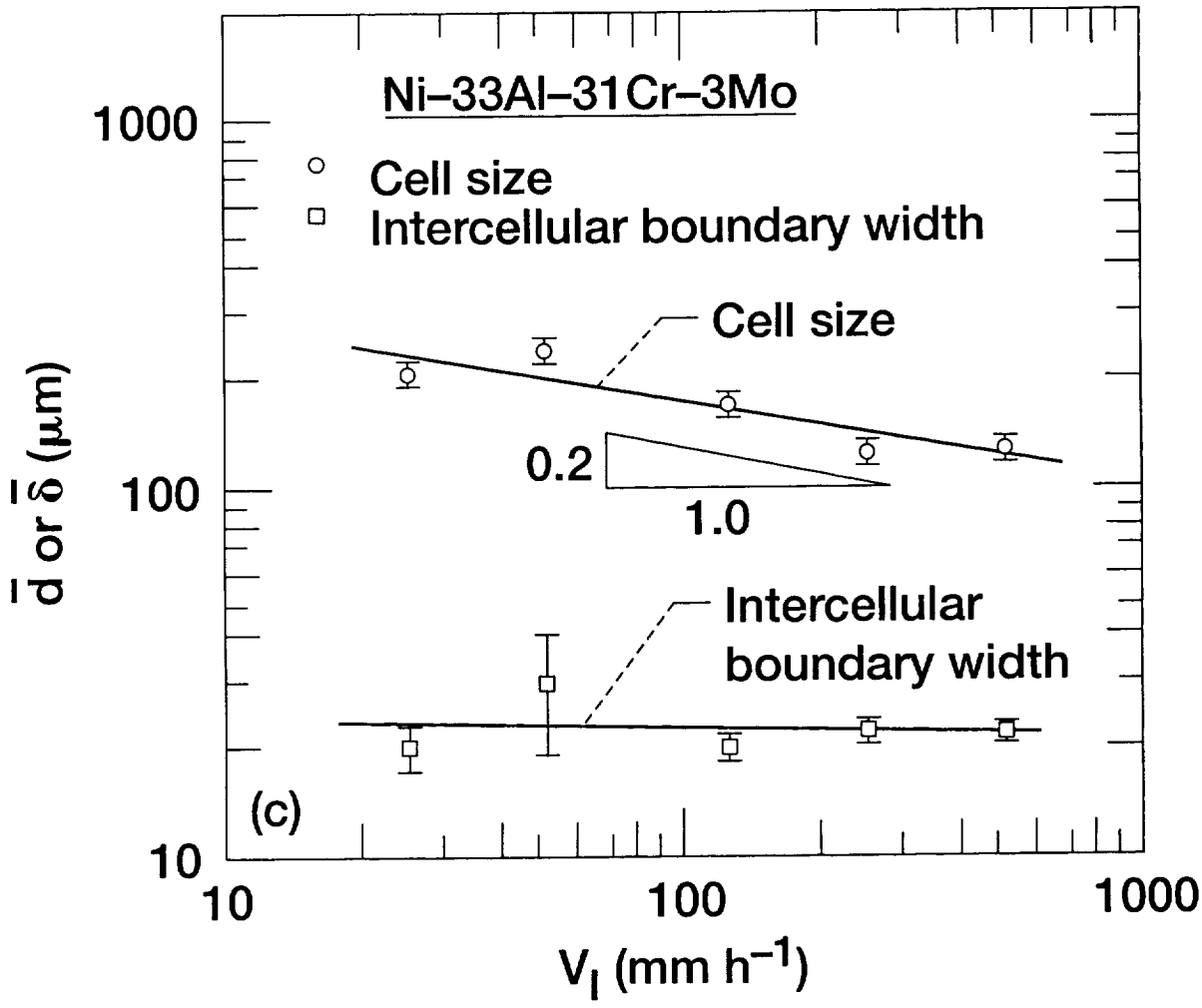
Ni–33Al–31Cr–3Mo
Cell size
Intercellular boundary width
Cell size
0.2
1.0
Intercellular
boundary width
(c)
1000
100
10
10
100
1000
$\bar{d}$ or $\bar{\delta}$ (μm)
V_I (mm h^{-1})

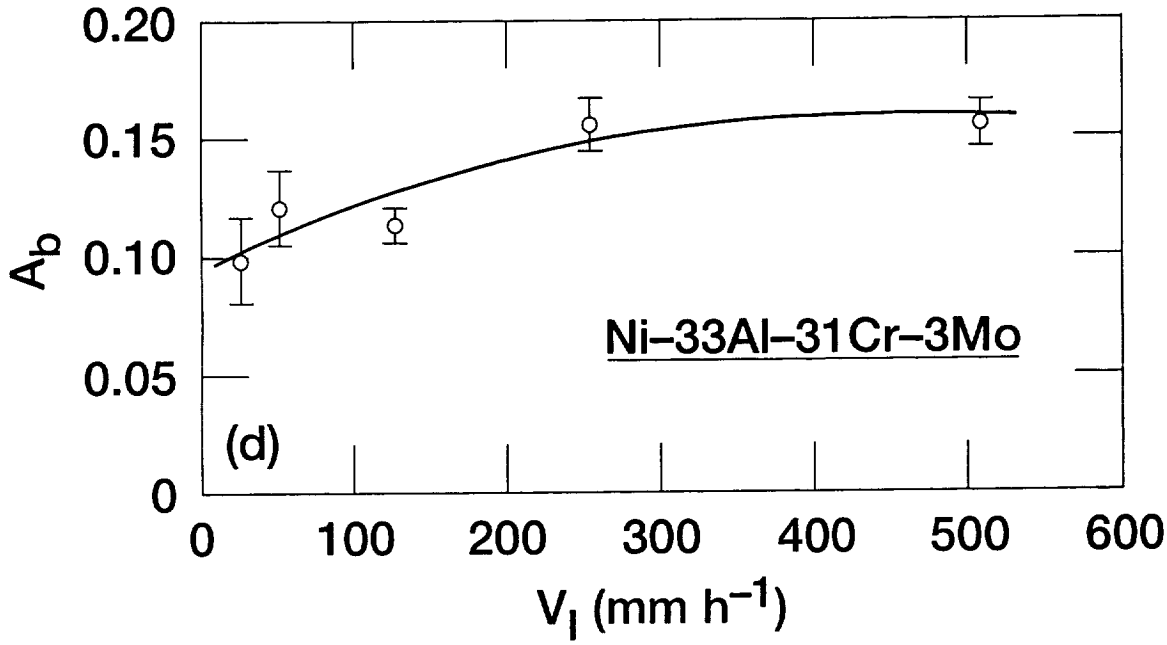
Ni–33Al–31Cr–3Mo
(d)
0.20
0.15
0.10
0.05
0
0
100
200
300
400
500
600
A_b
V_I (mm h^{-1})

Fig. 6c, d.

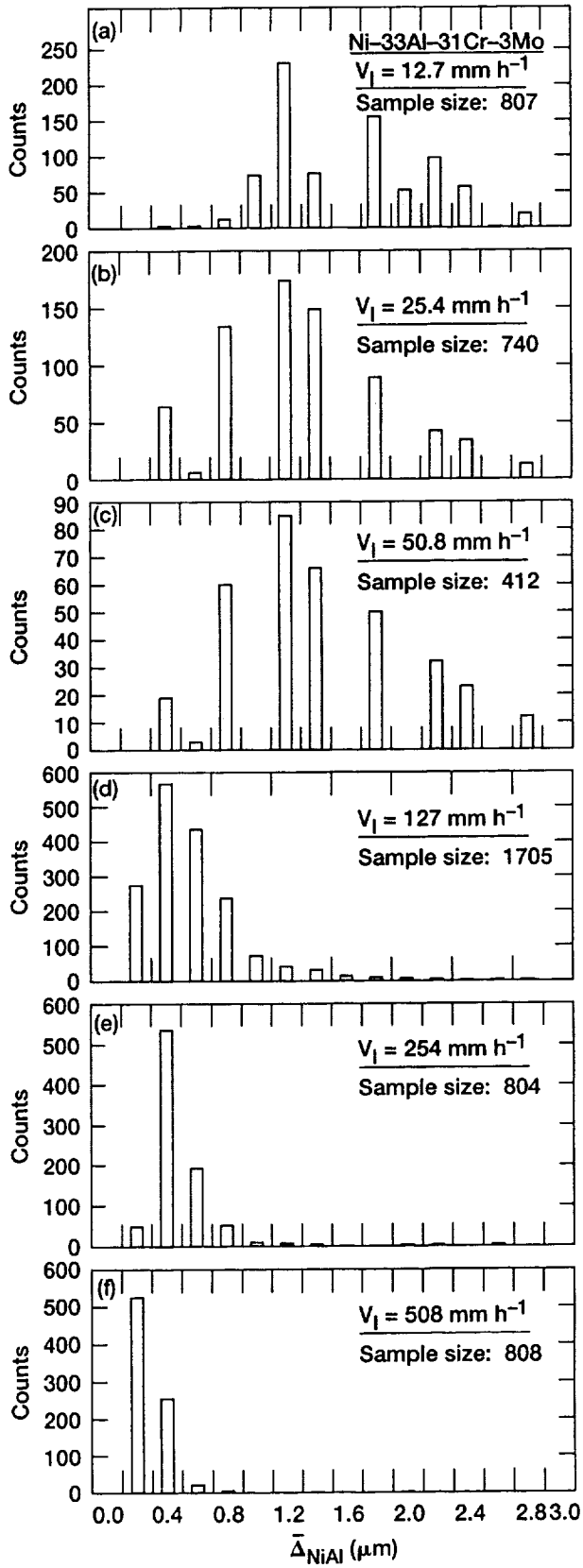
(a)
Ni–33Al–31Cr–3Mo
V_I = 12.7 mm h^{-1}
Sample size: 807
(b)
V_I = 25.4 mm h^{-1}
Sample size: 740
(c)
V_I = 50.8 mm h^{-1}
Sample size: 412
(d)
V_I = 127 mm h^{-1}
Sample size: 1705
(e)
V_I = 254 mm h^{-1}
Sample size: 804
(f)
V_I = 508 mm h^{-1}
Sample size: 808
Counts
0.0 0.4 0.8 1.2 1.6 2.0 2.4 2.83.0
$\bar{\Delta}_{NiAl}$ (μm)

Fig. 7.

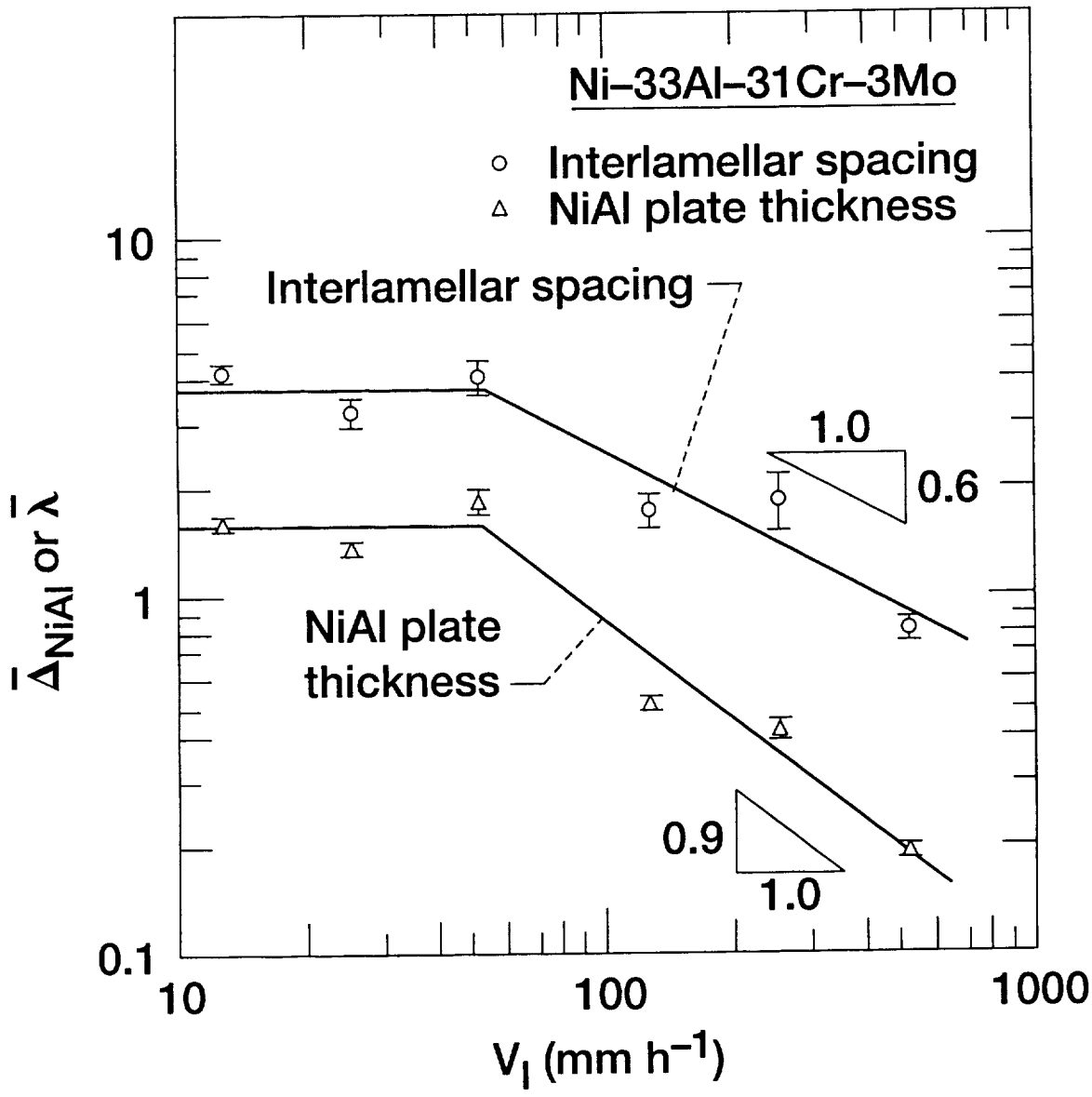
Ni–33Al–31Cr–3Mo
Interlamellar spacing
NiAl plate thickness
Interlamellar spacing
NiAl plate thickness
1.0
0.6
0.9
1.0
10
1
0.1
10
100
1000
$\bar{\lambda}$ or $\bar{\Delta}_{NiAl}$
V_I (mm h^{-1})

Fig. 8.

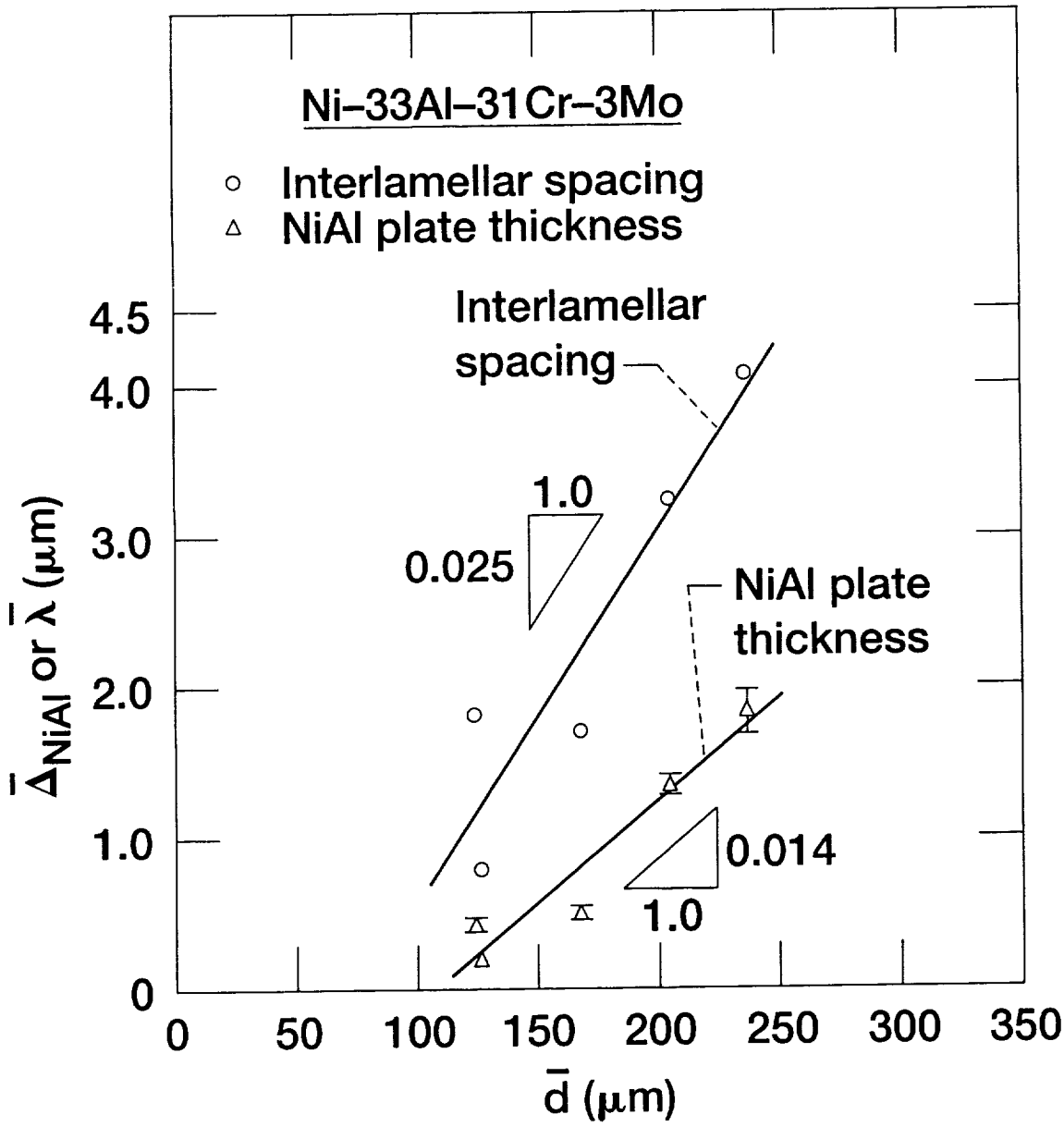
Ni–33Al–31Cr–3Mo
Interlamellar spacing
NiAl plate thickness
Interlamellar spacing
NiAl plate thickness
1.0
0.025
0.014
1.0
$\bar{\Delta}_{NiAl}$ or $\bar{\lambda}$ (μm)
$\bar{d}$ (μm)
0
1.0
2.0
3.0
4.0
4.5
0
50
100
150
200
250
300
350

Fig. 9.

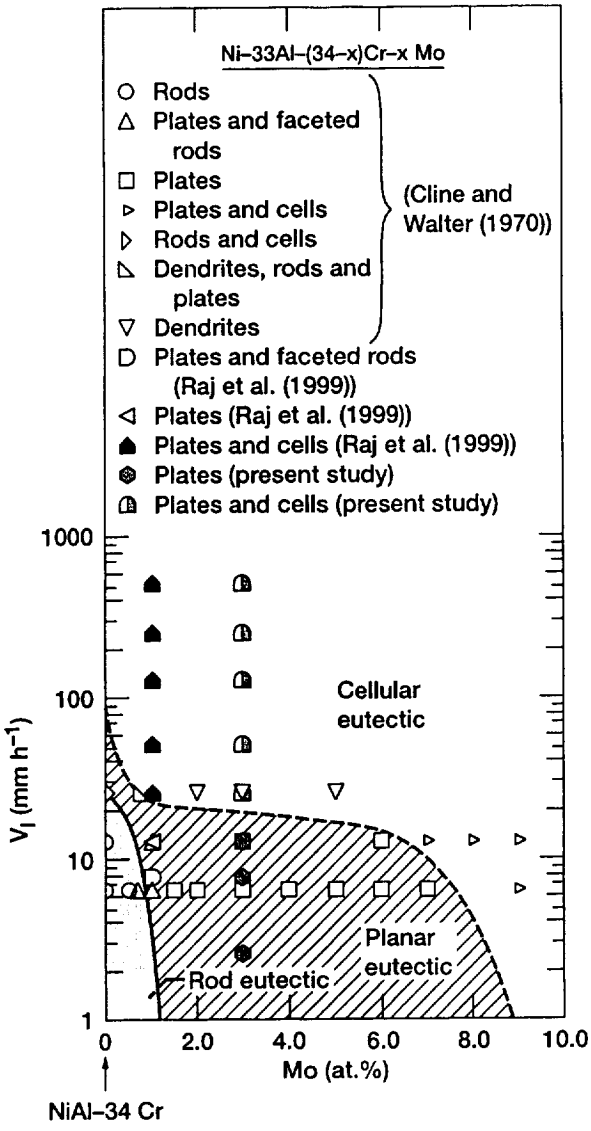
Ni–33Al–(34–x)Cr–x Mo
Rods
Plates and faceted rods
Plates
Plates and cells
Rods and cells
Dendrites, rods and plates
Dendrites
(Cline and Walter (1970))
Plates and faceted rods (Raj et al. (1999))
Plates (Raj et al. (1999))
Plates and cells (Raj et al. (1999))
Plates (present study)
Plates and cells (present study)
1000
100
10
1
V_I (mm h^{-1})
Cellular eutectic
Planar eutectic
Rod eutectic
0
2.0
4.0
6.0
8.0
10.0
Mo (at.%)
NiAl–34 Cr

Fig. 10.